Chemical Science

ROYAL SOCIETY OF CHEMISTRY

EDGE ARTICLE

View Article Online
View Journal | View Issue

Cite this: *Chem. Sci.*, 2025, **16**, 13082

All publication charges for this article have been paid for by the Royal Society of Chemistry

Received 18th March 2025
Accepted 10th June 2025

DOI: 10.1039/d5sc02092a

rsc.li/chemical-science

2D spatial structure-favored, tandem catalysis-boosted direct transformation of methane to methanol over Cu-FER†

Ning Liu, Tingting Zhang, Chengna Dai, Ruinian Xu, Gangqiang Yu, Ning Wang and Biaohua Chen *

The direct transformation of methane into methanol (DMTM) remains a significant challenge of C1 chemistry. Herein, we investigate continuous N_2O-DMTM over Cu-FER zeolite. A two-dimensional (2D) spatial structure-favored tandem catalysis is for the first time elucidated, which leads to boosted (CH_3OH + DME) productivity, corresponding to 2736 μmol g_{cat}^{-1} h^{-1} or 58 368 mmol per mol_{Cu} per h of CH_3OH, and improved reaction stability (passing through a 100 h long-term test). A unique dual Cu single-atom site located at the parallel 6-membered ring (MR) of the 8 MR channel could be generated, which serves as the primary CH_3OH production active site exhibiting much higher activity than the traditional monomeric $[Cu]^+$ and Cu dimer sites. The generated CH_3OH can subsequently diffuse from the 8 MR channel into a 10 MR main channel and directly react with the radicals of CH_3^- and OH^- to produce DME not only favoring DME production but also efficiently preventing carbon deposition. The present work highlights a tandem catalysis over Cu-FER that would substantially favor the design of other efficient catalysts for N_2O-DMTM.

Introduction

Direct transformation of methane to methanol (DMTM), being recognized as the holy grail of C1 chemistry, has attracted great attention.[1–3] In contrast to the traditional syngas route, which needs high temperature and pressure, DMTM, operated under mild conditions, is highly appealing.[2,4,5] However, the conflict between the exceptionally high C–H bond energy of CH_4 (413 kJ mol^{-1}) and the limited thermostability of CH_3OH leads to low CH_3OH productivity.[6] To address this issue, extensive efforts have been focused on developing highly efficient low-temperature catalysts[7] and utilizing alternative oxidants such as N_2O[8–12] and H_2O_2 (ref. 13 and 14) to enhance CH_3OH production. N_2O, known as a greenhouse gas, can be generated in large quantities from adipic acid chemical production, which produces one type of active oxygen species (named αO) through interaction with zeolite catalyst under mild conditions (around 250 °C).[11] Thereby, N_2O-DMTM, taking advantage of *in situ*-generated active αO, constitutes a promising approach to achieve high CH_3OH production.

The Cu-zeolites[10,15–20] have been widely investigated in DMTM. Various types of active sites have been reported, including monomeric $[Cu]^+$,[17,18] $[Cu–O–Cu]^{2+}$,[10] $[Cu_3O_3]^{2+}$ (ref. 19) and the newly reported extraframework $[Cu_2AlO_3]^{2+}$.[20] Most recently, it is reported that dual single-atom (SA) synergistic catalysis exhibits significantly higher reaction efficiency for DMTM relative to other catalyst systems.[13,21–23] For example, the synergistic interaction between the Cu–Ag dual SA active site on ZSM-5 facilitates the formation of highly reactive surface hydroxyl species and promotes the activation of C–H bond in CH_4.[13] A Cu pair dual SA located at the 8-rings of adjacent gme cavities of MAZ zeolite is reported to be favorable for O_2-DMTM.[21] A binuclear Fe(II) located at the adjacent six-membered ring (6 MR) of FER zeolite can split O_2 even at room temperature for DMTM.[22,23] Furthermore, it is also reported that regulation of the distance between the dual Cu SA sites as well as the proximity between Brønsted acid sites (BAS) and Cu active sites are crucial strategies to further enhance CH_3OH production,[24] due to the close proximity of the dual Cu SA site, which can lead to overoxidation of CH_3OH into CO_2, while the closely situated Cu site and BAS can facilitate the formation of hydrocarbons (C_xH_y) through further reaction of CH_3OH over the BAS site. Inspired by these literature reports, we can infer that leveraging the unique spatial structure of zeolite catalyst to create a highly efficient dual SA site would constitute a viable route for efficient DMTM catalyst design; meanwhile, selecting large porous topologized zeolites can

College of Environmental and Science Engineering, Beijing University of Technology, Beijing, 100124, China. E-mail: chenbh@bjut.edu.cn

† Electronic supplementary information (ESI) available: Additional descriptions of method as well as experimental and theoretical evidence, including activity measurement results, XRD, XAS, $k^3\chi(k)$ curve, ^{27}Al NMR, XPS, H_2-TPR, optimized DFT models, and microkinetic modelling results. See DOI: https://doi.org/10.1039/d5sc02092a

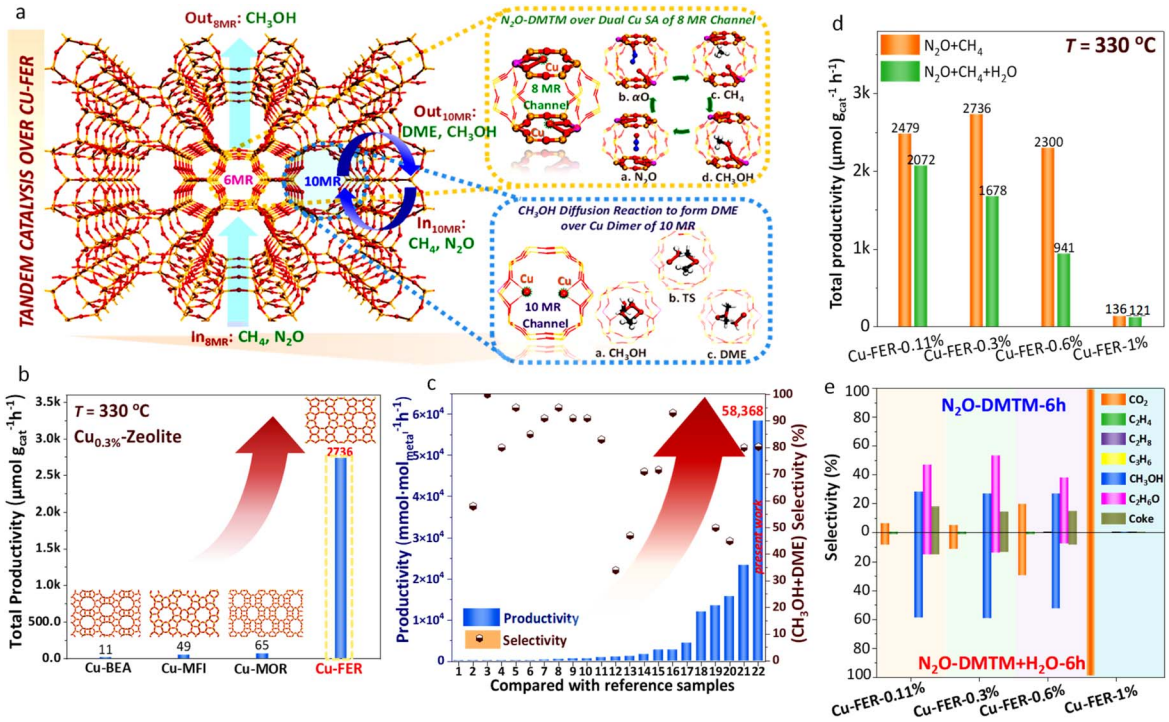

Fig. 1 Schematic diagram of N_2O-DMTM over Cu-FER and activity measurement results (T = 330 °C and t = 6 h). (a) A dual Cu SA site can be formed at the opposite 6 MR of the β site of the 8 MR channel, efficiently favoring αO formation, CH_4 activation and CH_3OH desorption. The CH_3OH would diffuse from the 8 MR channel into the 10 MR channel and readily react with CH_3^- and OH^- radicals, generated over the Cu dimer ($[Cu]^+$–$[Cu]^+$), to produce DME. (b) Total productivity (CH_3OH + DME) comparison over Cu-zeolite (BEA, MFI, MOR and FER) with Cu loading of 0.3 wt% (average value after 6 h reaction). (c) Productivity comparison with recent literature report of continuous DMTM (see Table S1†). (d) Total (CH_3OH + DME) productivity comparison over Cu-FER with diverse Cu loadings (0.11, 0.3, 0.6 and 1.0 wt%) in the absence and presence of H_2O (10 vol%). (e) Product selectivities corresponding to activity measurements in panel (d); reaction conditions: $N_2O/CH_4/He/(H_2O)$ = 30 : 15 : 55(45) : (10), with gas hourly specific velocity (GHSV) = 12 000 h^{-1}, m_{cat} = 0.5 g; other activity measurement results are profiled in Fig. S1a–e and 3a–f.† The total productivity, encompassing both CH_3OH and DME, was calculated by considering one mole of DME as equivalent to two moles of CH_3OH.

increase the distance between active site and BAS to mitigate excessive production of C_xH_y byproducts.[24]

In the present work, a series of Cu-modified zeolites with different topological structures (FER, BEA, MFI, MOR, Si/Al ≈ 15, Cu = 0.3 wt%) were prepared by wet ion-exchange method and investigated for continuous N_2O-DMTM (Fig. 1b and S1a–e†). Boosted productivity can be achieved for the Cu-FER-0.3%, being two orders of magnitude higher than the other counterparts (2736 *versus* 11–65 μmol g_{cat}^{-1} h^{-1}, Fig. 1b), and which also notably exceeds most of the recently reported studies (58 368 mmol mol_{Cu}^{-1} h^{-1}, Fig. 1c and Table S1†). This indicates an exceptionally higher reaction efficiency of the loaded copper species over Cu-FER-0.3%. Additionally, long-term stability is evident (Fig. S2a†), with CH_3OH productivity remaining at approximately 1540 μmol g_{cat}^{-1} h^{-1} (32 853 mmol mol_{Cu}^{-1} h^{-1}) even after 100 h of testing. A 2D (two-dimensional) zeolitic spatial structure-favored tandem catalysis is for the first time unravelled over Cu-FER-0.3% (Fig. 1a). Briefly, favored by the 2D spatial structure of FER, a unique dual Cu SA site is formed at the parallel 6 MR site of the 8 MR channel, which possesses much higher CH_3OH production efficiency than the traditional $[Cu]^+$ monomer and $[Cu]^+$–$[Cu]^+$ dimer sites. Subsequently, the generated CH_3OH could diffuse into the 10 MR channel for tandem catalysis to produce dimethyl ether (DME), wherein the CH_3OH, functioning as a "solvent," can directly react with the radicals of CH_3^- and OH^-, which not only promotes DME production but also efficiently hinders carbon deposition. Generally, the present work presents an efficient, continuous N_2O-DMTM system based on Cu-FER zeolite and provides profound mechanistic insights, which would substantially favor other highly efficient catalyst designs.

Results and discussion

N_2O-DMTM over Cu-FER with varying Cu loadings and basic characterizations

The influence of Cu loading (0.11–1 wt%) was also investigated for the N_2O-DMTM in the absence and presence of H_2O (Fig. 1d, e and S3a–f†), which suggests an optimum Cu loading of 0.3 wt% with the highest CH_3OH productivity and (CH_3OH + DME) selectivity of 80.3% (in the absence of H_2O) and 73.4% (in the presence of H_2O), respectively (Table S2†). Comparable CH_4 conversions (Fig. S3f†) can be found over the samples of Cu-FER-0.11%, 0.3% and 0.6% (4.6, 4.7 and 4.8% of N_2O-DMTM and 3.9, 3.2 and 2.3% of N_2O-DMTM-H_2O) with relatively low Cu loadings. However, a significant increase in CH_4 conversions

(50.3% and 49.7%) is evident for the Cu-FER-1% sample during both N_2O-DMTM and N_2O-DMTM-H_2O. This enhancement is closely related to the overoxidation of CH_4, resulting in substantial CO_2 production, displaying a high CO_2 selectivity of 99.1 (N_2O-DMTM) and 99.2% (N_2O-DMTM-H_2O), as shown in Fig. 1e. This finding indicates that there would exist competing pathways ($N_2O \rightarrow N_2 + O_2$), leading to the over-oxidation of CH_4, which is closely correlated with the coordination environment of Cu species (CuO_x over Cu-FER-1%, as unravelled by H_2-TPR). Notably, H_2O alters the reaction selectivity, with CH_3OH being the dominant product when H_2O is present, while dimethyl ether (DME) predominates during its absence. This can be closely correlated with the specific reaction mechanism, which will be further discussed later.

To characterize the chemical states of the loaded Cu species over Cu-FER samples, X-ray diffraction (XRD), XPS, and H_2-TPR were conducted. The XRD patterns (Fig. S4†) primarily display peaks characteristic of the FER framework, with no distinct peaks attributable to CuO_x species. The XPS spectra (Fig. 2a) show that the surface Cu species are predominantly in the +2 oxidation state, evidenced by the Cu $2p_{3/2}$ binding energy at 933.5 eV.[10,25] Shake-up satellite peaks around 945.4 eV for the samples with Cu loading above 0.6% and 944.0 eV for Cu-FER-0.3% were observed, indicating the presence of Cu^{2+} species.[25] No obvious XPS signals related to CuO_x species (936 eV[10]) could be detected, which suggests that the CuO_x species, (as detected by H_2-TPR of Cu-FER-0.6% and 1.0%, Fig. 2b), are highly dispersed and does not form large, detectable crystalline domains. As noted, no Cu^+ species were detected, which commonly display the lower Cu $2p_{3/2}$ peak at around 932 eV. H_2-TPR results (Fig. 2b) further reveal that Cu^{2+} cations are the predominant species in samples with lower Cu loadings (0.11 and 0.3 wt%). In contrast, CuO_x species gradually form in samples with higher Cu loadings (0.6 and 1.0 wt%). This finding

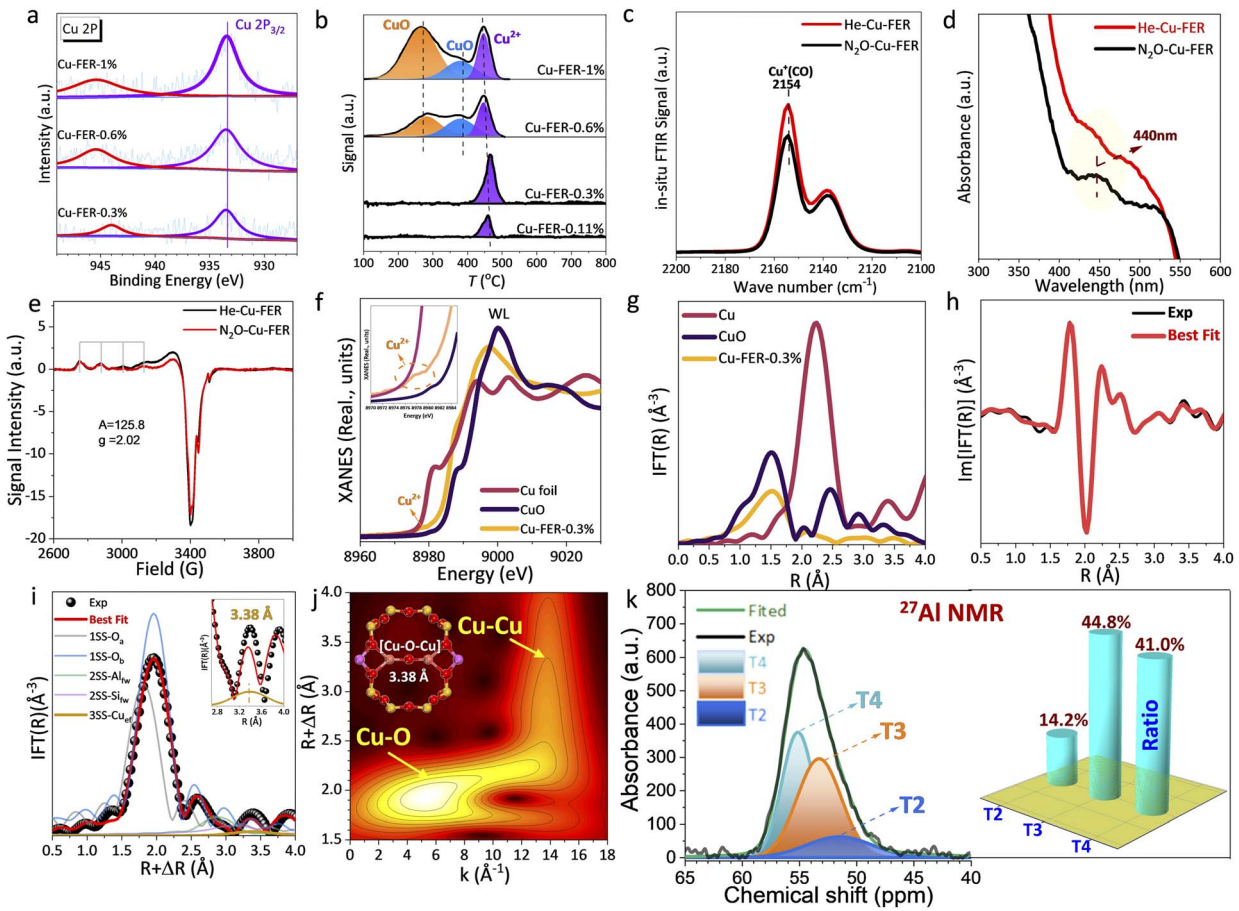

Fig. 2 Physicochemical characterizations of Cu-FER samples with various Cu loadings (0.11, 0.3, 0.6, and 1%). (a) XPS, (b) H_2-TPR, and (c) CO-probed *in situ* Fourier transform infrared spectroscopy (FTIR); (d) UV-vis diffuse reflectance spectroscopy (UV-vis DRS); and (e) electron paramagnetic resonance (EPR). He–Cu-FER in panels (c–e) represents the Cu-FER-0.3% being pretreated at 500 °C under a He atmosphere (>99.999%, 40 mL min^{-1}) for 1 h; N_2O–Cu-FER represents Cu-FER-0.3% initially pretreated by He (following the above procedure) and then further treated by N_2O (30 vol% N_2O in He) at 250 °C for 1 h. (f) Cu K-edge X-ray adsorption near-edge spectra (XANES) and (g) Fourier-transformed extended X-ray absorption fine structure (FT-EXAFS) spectra of N_2O-pretrated Cu-FER-0.3%, Cu foil and CuO; (h) imaginary and (i) magnitude part of phase-corrected FT-EXAFS spectra for N_2O-pretrated Cu-FER-0.3% obtained by Fourier transforming the $k^3\chi(k)$ curves in Fig. S5† of 2.4–10.8 Å. (j) The wavelet transform of k^3-weighted EXAFS spectra; the lobes corresponding to Cu–O and Cu–Cu scattering contributions are pointed out with arrows. (k) The ^{27}Al nuclear magnetic resonance (NMR) spectra of Cu-FER-0.3 and predicted contents of different Al location sites based on peak area integration.

aligns with the decreased product selectivity (Fig. 1e) observed in Cu-FER samples with higher Cu loading (0.6 and 1.0 wt%), due to the formation of CuO species that readily promote CH_4 overoxidation.[10] Furthermore, quantitative H_2-TPR analysis, based on H_2 consumption of standard CuO (Table S3†), corroborates the identification of Cu species in the Cu-FER samples. As noted, the loaded Cu species commonly exist in two different states over the Cu-modified zeolites: CuO_x oxidation state and Cu^{2+} cation state (being exchanged with the Brønsted acid site). These two types of Cu species are distinguishable by H_2-TPR due to different redox abilities. The CuO_x species would be much more easily reduced relative to the Cu^{2+} cation, which is commonly ion-exchanged inside the zeolite channel and is relatively harder to be reduced. As for the CuO_x species, the small-particle CuO_x would be much more readily reduced than bulk CuO_x, thereby displaying two types of reduction peaks in Fig. 2b over the samples of Cu-FER-0.6% and Cu-FER-1%.

Based on the above basic characterizations, the Cu cations constitute the active species over Cu-FER-0.3%. The Cu cations typically exist as monomeric $[Cu]^+$ or a Cu dimer (adjacent $[Cu]^+$–$[Cu]^+$ that can evolve into $[Cu–O–Cu]^{2+}$ following oxidation) within the Cu-zeolite.[15,16,18,24,26,27] To make a further identification, CO-probed FTIR, UV-vis DRS and EPR were initially employed to characterize Cu-FER-0.3%, wherein the sample was respectively pretreated by He and N_2O, denoted as He–Cu-FER and N_2O–Cu-FER, for better comparison. A characteristic CO adsorption vibration band over the monomeric $[Cu]^+$ site (ν_{CO} = 2154 cm^{-1}) was clearly observed (Fig. 2c),[10] and the band intensity of N_2O–Cu-FER was decreased to a certain degree relative to He–Cu-FER. This finding indicates the coexistence of both monomeric $[Cu]^+$ and Cu dimer ($[Cu]^+$–$[Cu]^+$). The Cu dimer can be oxidized into $[Cu–O–Cu]^{2+}$ by N_2O, eventually leading to the observed decrease of ν_{CO} band at 2154 cm^{-1}. Notably, the Cu^+ cations detected by CO-probed *in situ* FTIR (Fig. 2c) can be closely related to the auto-reduction of Cu^{2+} cations during high-temperature (T = 500 °C) He pretreatment. Further pretreatment by N_2O (T = 250 °C) would lead to the formation of $[Cu–O–Cu]^{2+}$ by the neighboring monomeric $[Cu]^+$, eventually resulting in the decreasing vibration peak intensity. UV-vis DRS and EPR corroborate this finding, wherein the N_2O–Cu-FER shows a characteristic $[Cu–O–Cu]^{2+}$ UV-vis peak at ~440 nm (Fig. 2d),[28] aligning with its decreased intensity seen in EPR (Fig. 2e) due to the EPR-silent nature of $[Cu–O–Cu]^{2+}$. Taking advantage of this, the Cu dimer content was further predicted by EPR,[10] accounting for 20 wt% of Cu over Cu-FER-0.3%.

To further identify such oxo-Cu dimer motif structure ($[Cu–O–Cu]^{2+}$), the N_2O–Cu-FER was characterized using XAS. The Cu K-edge XANES (Fig. 2f) displayed a distinct pre-edge peak at approximately 8978 eV, which is characteristic of the 1s–3d transition in Cu^{2+} [10,17], indicating dominant Cu^{2+} species in Cu-FER-0.3%. The white line (WL) intensity is greater than that of Cu foil, yet lower than that of CuO, suggesting the Cu species is in a less oxidative environment compared to CuO. Moreover, a distinct FT-EXAFS spectrum was observed for Cu-FER-0.3%, in contrast to CuO and Cu foil (Fig. 2g). The EXAFS fitting (Fig. 2i, S6 and Table S4†), combined with wavelet transform (WT) analysis (Fig. 2j), further confirmed the existence of $[Cu–O–Cu]^{2+}$, which shows a Cu–Cu distance of 3.38 Å, wherein the EXAFS-WT clearly displays two lobes, at low (2.5–7.5 $Å^{-1}$) and high (10–15 $Å^{-1}$) k ranges, being respectively associated with framework O/Si/Al and Cu–Cu contribution in the oxygen-bridged Cu dimer.[29] Meanwhile, the EXAFS-WT indicated that the Cu species is majorly located at the ion-exchange site being coordinated by the framework O. Notably, density functional theory (DFT) calculations were conducted to determine the site of such Cu dimer (Fig. S7†), which indicated that the Cu dimer site is energetically favorable to be located at the opposite T3 site of 10 MR, and such structure was utilized for the EXAFS peak fitting.

Next, ^{27}Al NMR was conducted to elucidate the specific location of Al atoms and related occupation ratios over Cu-FER-0.3%. The ^{27}Al NMR spectrum (Fig. S8†) displays a prominent signal around 55 pm, with no significant signals detected between 20–40 ppm indicative of extra-framework Al,[8] which indicates that the Al atoms are primarily located within the framework.[30] Moreover, the resonance band can be deconvoluted into three distinct bands (Fig. 2k), attributable to framework Al located at T2 (51.5 ppm), T3 (53.3 ppm), and T4 (55.2 ppm).[31] The specific ratio was accordingly predicted based on the peak area integral, which revealed that the framework Al is mainly located at the T3 (44.8%, 10 MR channel) and T4 (41.0%, 8 MR channel) sites. This finding indicated that the T3 and T4 sites act as major potential sites for Cu accommodation over Cu-FER-0.3%, which well supports the DFT calculation (Fig. S7†) pinpointing the Cu dimer site at the T3 position of the 10 MR ring.

N_2O-DMTM over traditional monomeric $[Cu]^+$ and Cu dimer ($[Cu]^+$–$[Cu]^+$) site

To uncover the reason for the boosted N_2O-DMTM performance of Cu-FER, DFT was initially employed to simulate N_2O-DMTM over the monomeric $[Cu]^+$ and Cu dimer ($[Cu]^+$–$[Cu]^+$) sites of Cu-FER and with the calculated energy barrier (ΔE) being compared with those of Cu-BEA[10] and Cu-ZSM-5 (ref. 32) in our previous works (see Fig. 3a). As noted, the radical mechanism was simulated by DFT, as revealed by *in situ* FTIR study (Fig. S9a and b†), which is also consistent with our previous reports.[10,32] As shown in Fig. 3a, comparable energy barriers can be observed for both scenarios of the monomeric $[Cu]^+$ and Cu dimer sites of Cu-FER relative to other topologized zeolites. This finding indicates that the zeolitic topology structure would exert limited effect on the intrinsic N_2O-DMTM efficiency of the traditional monomeric $[Cu]^+$ and Cu dimer sites. Such discrepancy with the boosted CH_3OH productivity of Cu-FER (Fig. 1b) implies that there must exist some other super active site over Cu-FER.

Carefully analyzing the energy diagrams in Fig. 3a and c, one can find that the monomeric $[Cu]^+$ site possesses much lower barriers in CH_4 activation (TSII), CH_3^-, OH^- radical rebound (TSIII), and CH_3OH desorption steps (0.12, 0.42 and 1.12 eV, Cu-FER) than the Cu dimer (0.49, 0.64 and 1.58 eV, Cu-FER);

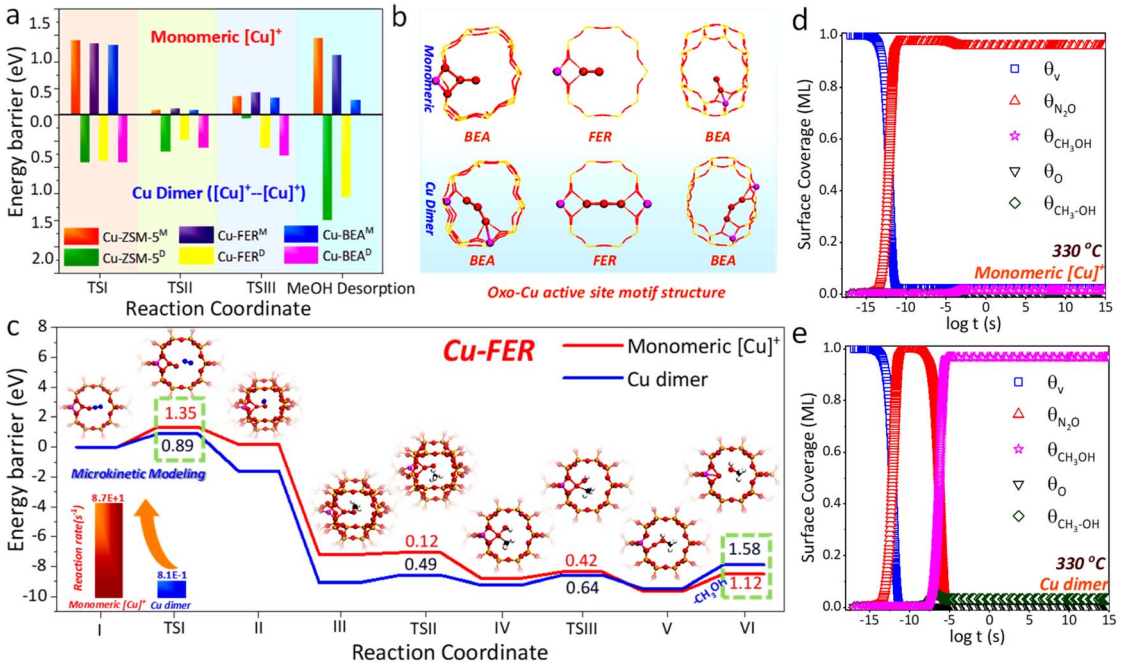

Fig. 3 DFT and microkinetic modeling results of N_2O-DMTM. (a) Energy barrier comparisons of Cu-FER with other topologized Cu-zeolites (BEA[10] and MFI[32]) in our previous works; the superscript ^{M} indicates the Cu monomeric site, and ^{D} represents the Cu dimer. (b) Optimized oxo-Cu active site motif structures. (c) Energy diagram over the monomeric $[Cu]^+$ and Cu dimer sites of Cu-FER and reaction rate comparisons derived by microkinetic modelling (Tables S5 and S6†); the optimized models are depicted in Fig. S10 and S11,† and the monomeric $[Cu]^+$ active site model is inset in panel (c) for a better display. O red, Cu orange, Al pink, Si yellow, C gray, H, white. (d and e) Surface coverage variations along time t derived by microkinetic modeling of (d) monomeric $[Cu]^+$ and (e) the Cu dimer of Cu-FER; as noted, the opposite T3 site (Fig. S7†) and single T3 site (Fig. S12†) in the 10 MR channel were selected as the energetically favorable sites for Cu dimer and monomeric $[Cu]^+$, respectively.

however, it displays a notably higher barrier in the initial N_2O dissociation step (TSI, 1.35 *versus* 0.89 eV, Cu-FER). Microkinetic modelling (Fig. 3c–e, Tables S5 and S6†) further indicates a much higher reaction efficiency of the monomeric $[Cu]^+$ site, with the reaction rate being two orders of magnitude higher than the Cu dimer (8.7×10^1 *versus* 8.1×10^{-1} s^{-1}, Fig. 3c). Meanwhile, the N_2O dissociation step serves as the rate-determining-step (RDS) over the monomeric $[Cu]^+$ site (Fig. 3d), and the CH_3OH desorption step (Fig. 3e) constitutes the RDS of the Cu dimer site, with the surface-adsorbed N_2O (θ_{N_2O}) and CH_3OH (θ_{CH_3OH}) respectively constituting the major surface species. In this regard, we speculate that the boosted N_2O-DMTM activity could be probably achieved if the N_2O dissociation barrier can be extensively reduced over the monomeric $[Cu]^+$ site of Cu-FER.

N_2O-DMTM over dual Cu SA site

According to the pioneering work of Sobalik's group[33,34] a distinct Fe cation accommodation site within the FER zeolite has been reported, which allows for the placement of two Fe cations at the parallel 6 MR plane (β site) by the Al pair, with a $[Fe]^{2+}$–$[Fe]^{2+}$ distance of 7.4 Å, consequently leading to significantly higher N_2O dissociation activity of Fe-FER relative to Fe-ZSM-5 and Fe-BEA, due to the synergistic effect of distant $[Fe]^{2+}$. Favored by this, Fe-FER has also been extended to O_2-DMTM.[22,23] Inspired by these literature reports, we supposed that there probably also exists a similar accommodation site for the $[Cu]^+$ cations that can efficiently favor N_2O dissociation. However, the large $[Cu]^+$–$[Cu]^+$ distance complicates the site's identification, rendering it "invisible" to extended X-ray absorption fine structure (EXAFS) or diffraction experiments.[35] Therefore, to shed more light, *ab initio* molecular dynamics (AIMD) was employed in the present work to simulate N_2O-DMTM over a constructed Cu-FER model featuring two $[Cu]^+$ cations positioned on a parallel 6 MR plane (β site) (Fig. 1a, $d_{[Cu]^+-[Cu]^+} = 7.49$ Å). Notably, each $[Cu]^+$ is coordinated by one AlO_4^- of the T4 site that has been confirmed as a primary location site for Cu cations based on ^{27}Al NMR (Fig. 2k). We refer to this active site as a "dual Cu SA site" to distinguish it from the Cu dimer site.

A remarkably low Gibbs free energy barrier of only 0.26 eV needs to be crossed to generate αO over such dual Cu SA site (Fig. 4a, b, d and Movie S1†), which is substantially lower than the ΔG values of 1.33 and 0.76 eV for the monomeric $[Cu]^+$ and Cu dimer site, respectively. Moreover, due to the extended $[Cu]^+$–$[Cu]^+$ distance, a new motif structure of ($[Cu–O]^+$–$[Cu]^+$, II in Fig. 4a) could be evolved, wherein the subsequent DMTM reaction, including CH_4 activation, CH_3OH formation and desorption, occurs over the monomeric $[Cu–O]^+$ site by crossing a low Gibbs free energy barrier of 0.33 eV (Fig. 4a, c, e and Movie S2†), and the distant $[Cu]^+$ acts as an observer in these steps. The microkinetic modelling (Fig. 4f) further reveals a significantly promoted reaction rate of such dual Cu SA site (5.64×10^8 s^{-1}), which is respectively six and eight orders of magnitude

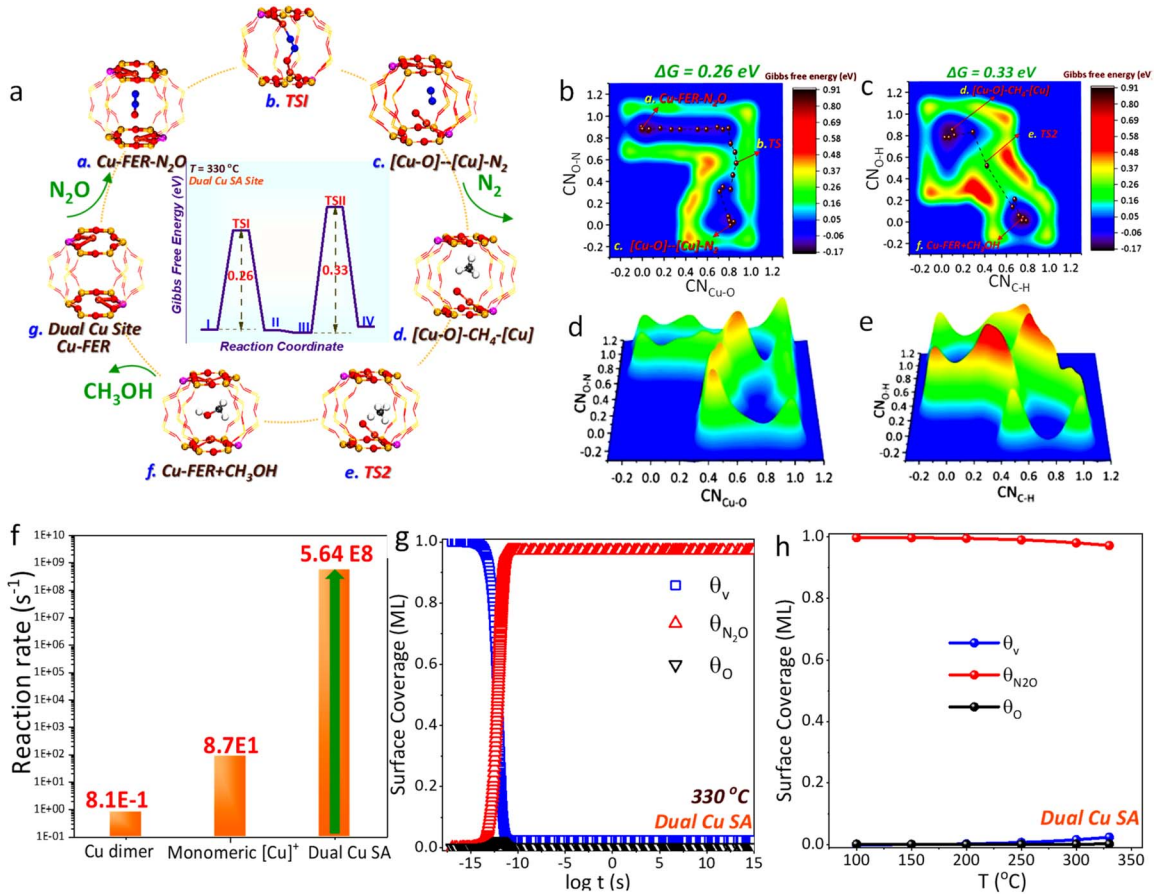

Fig. 4 AIMD simulation results and microkinetic modeling outcomes of N_2O-DMTM over the dual Cu SA of the Cu-FER zeolite. (a) Derived energy diagram along with reaction coordinate. (b–e) 2D and 3D free energy surface of the (b and d) N_2O dissociation to generate αO and (c and e) CH_4 activation over the $[Cu–O]^+$–$[Cu]^+$ site to generate CH_3OH; O red, Cu orange, Al pink, Si yellow, N blue, C gray, H, white. (f) Reaction rate comparisons of monomeric $[Cu]^+$, Cu dimer and dual Cu SA site derived by microkinetic modelling. (g and h) Surface coverage variations along with simulation time t at $T = 330$ °C (g) and equilibrium surface coverage as a function of reaction temperature T (h) over the dual Cu site of Cu-FER based on microkinetic modelling (Table S7†). As noted, the conversion of structure d to e only involves one transition state (TS), while two types of TS need crossing in Fig. 3. Such diverse reaction routes can be closely related to the different simulation approaches applied (AIMD, Fig. 4, and DFT, Fig. 3). Specifically, metadynamics was employed during the AIMD simulation to screen the Gibbs free energy surface along with two types of collective variables, wherein the reaction temperature was also taken into account by *NVT* ensemble, while the CI-NEB (climbing image nudged elastic band) approach was employed in searching the TS based on the widely reported radical rebound mechanism, thereby totally involving two TS.

higher than those of the traditional monomeric $[Cu]^+$ (8.7×10^1 s^{-1}) and Cu dimer (8.1×10^{-1} s^{-1}) site to produce CH_3OH. This finding fits well with the boosted activity of Cu-FER, which indicates that such dual Cu SA site would constitute a highly probable candidate active site during N_2O-DMTM over Cu-FER. Thereby, in light of the above AIMD simulation and microkinetic modelling, we can infer that favored by the unique topology structure of FER, leading to the formation of such highly active dual Cu SA site, on one hand, it significantly favors N_2O dissociation to generate αO through the synergistic effect between distant $[Cu]^+$ sites; and on the other hand, it efficiently prevents the formation of oxo-Cu dimers ($[Cu–O–Cu]^{2+}$) that possess much lower DMTM reaction efficiency than the evolved monomeric oxo Cu cation site of ($[Cu–O]^+$–$[Cu]^+$).

According to the above microkinetic modelling result, we can deduce that the N_2O dissociation step is the RDS over the dual Cu SA site during N_2O-DMTM, with the surface-adsorbed N_2O (θ_{N_2O}) constituting the major species (Fig. 4g). N_2O-DMTM over Cu-FER-0.3% was further conducted at $T = 330$ °C using N_2O/CH_4 ratios of 0.5 : 1 and 1 : 1. The (CH_3OH + DME) production rates were then accordingly calculated and compared with those derived from the scenario of $N_2O/CH_4 = 2 : 1$, attempting to identify such dual Cu SA site by investigating the kinetic effects of reactant pressures, as shown in Fig. S14.† As can be seen, the production rate of (CH_3OH + DME) obviously increased along with the increase of N_2O/CH_4 ratio, from 953, 1532 to 2736 μmol g_{cat} h^{-1}. This finding kinetically verifies the existence of the dual Cu SA site due to the N_2O dissociation step constituting the RDS over the dual Cu SA site, and thereby, increasing the CH_4 partial pressure would favor an increased reaction rate. As noted, although the monomeric $[Cu]^+$ also displays the RDS step of the N_2O

dissociation step, it can be ruled out due to its low reaction efficiency (8.7×10^{1} s^{-1}).

(a) Tandem catalysis of CH_3OH over BAS site. As widely reported,[36,37] DME could be generated through the reaction of CH_3OH molecules over the Brønsted acid site (BAS) following two competitive routes, known as the sequential and associative routes. The AIMD simulation result (Fig. 5 and Movie S3†) reveals that CH_3OH would primarily follow the associative route to generate DME over the BAS of Cu-FER by crossing much lower energy barriers than the sequential route (Fig. S15a†). Initially, the BAS would activate one approaching CH_3OH molecule by reacting with its hydroxyl group to form $[CH_3OH_2]$. Then, the $[CH_3OH_2]$ can further react with another diffusing CH_3OH by attacking its $[OH^-]$ group *via* the end H. After crossing two small energy barriers ($\Delta G = 0.22$ and 0.02 eV of TS1 and TS2, $T = 330$ °C of Fig. 5a and b), CH_3OH is converted into the CH_3^- radical and H_2O. Finally, CH_3^- interacts with CH_3OH to form another intermediate, namely CH_3OHCH_3, which is easily transformed into DME upon the removal of H over the AlO_4^- site to regenerate BAS. As noted, the $^{c}CN_{O-H}$ in Fig. 5c monitors the O–H bond of the Brønsted acid site H and framework O, which is initially reduced from ~0.8 to 0 and then increased to ~0.8, again representing the regeneration of the BAS site.

(b) Tandem catalysis of CH_3OH over monomeric $[Cu]^+$ and Cu dimer site. In addition to the BAS-DME route, most importantly, we identified an alternative route for dimethyl ether (DME) production, termed the Cu-active-site DME route (CAS-DME), which can occur over the Cu dimer and monomeric $[Cu]^+$ sites within 10 MR channels. As revealed by DFT, CH_3OH could directly react with the generated radicals of CH_3^- and OH^- to produce DME and release H_2O by crossing the low energy barriers of 0.69 eV (Cu dimer site, Fig. 6a) and 0.02 eV (monomeric $[Cu]^+$, Fig. S16a†), respectively. After that, the generated DME can readily desorb (0.49 and −0.08 eV) to regenerate the active site. The microkinetic modelling results (Tables S8 and S9†) demonstrate that DME production is significantly favored over the Cu dimer site, displaying a net reaction rate of 1.39×10^{6} s^{-1} (Fig. 6b), which is six orders of magnitude higher than the CH_3OH production rate (8.1×10^{-1} s^{-1}); however, comparable net reaction rates can be observed over the monomeric $[Cu]^+$ site (8.7×10^{1} and 8.9×10^{1} s^{-1}, Fig. S16b†). This disparity is primarily due to the tandem catalysis of methanol, which shifts the RDS from methanol desorption (Fig. 3e) to nitrous oxide (N_2O) dissociation (Fig. 6c) over the Cu dimer site. Conversely, the initial N_2O dissociation remains the RDS for the monomeric $[Cu]^+$ site (Fig. 3d and S16c†).

Furthermore, it should also be noted that the tandem CAS-DME pathway exhibits a relatively higher energy barrier and lower reaction rate (0.69 eV and 1.39×10^{6} s^{-1} in Fig. 6a and b over the Cu dimer site) compared to the CH_3OH production pathway (0.26 and 0.33 eV; 5.68×10^{8} s^{-1} in Fig. 4a and f over dual Cu SA site). This would influence the CH_4 oxidation to methanol to some extent, which however does not constitute a determining factor. As revealed by AIMD, the generated CH_3OH can be easily desorbed from the dual Cu SA site and would either be released as the final product from Cu-FER or participate in the subsequent tandem catalysis for DME production. In this regard, CH_4 oxidation into CH_3OH would primarily correlate with the RDS step of N_2O dissociation, consequently significantly affecting the generation rate of DME. The *in situ* FTIR, with He-pretreated Cu-FER-0.3% being initially exposed to (N_2O + CH_4) followed by He sweeping and interaction with CH_3OH, can well support the proposed CAS-DME

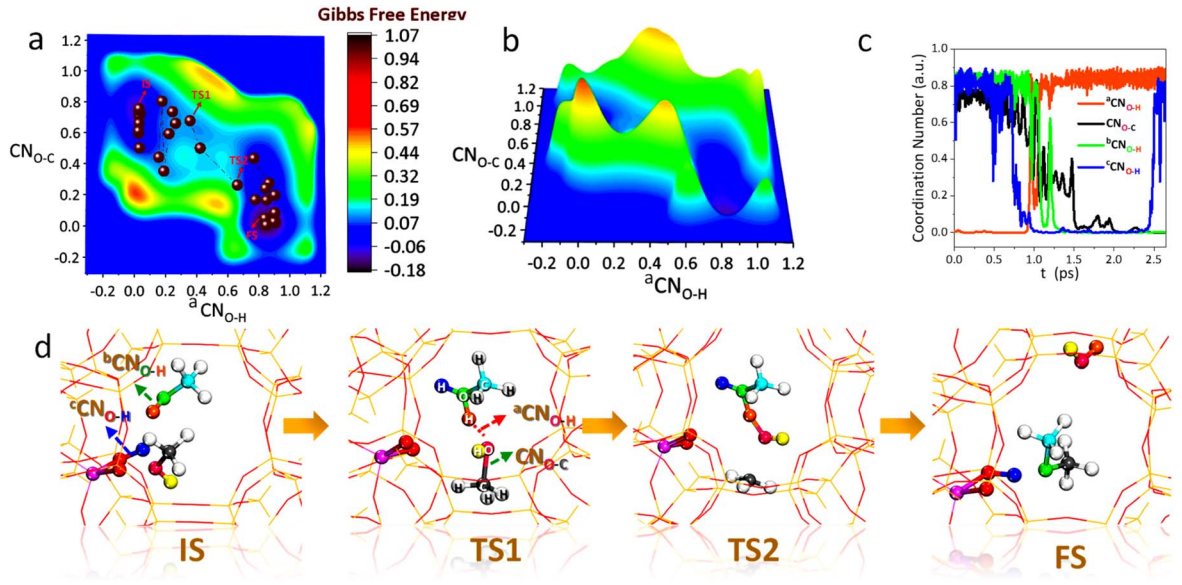

Fig. 5 AIMD simulation of the DME associative production route over the BAS site. (a and b) 3D and 2D free energy surface as function of the coordination number (CN) of O–C and ^{a}O–H, as illustrated in panel (d) of the TS1 model; a value of CN close to 1 represents bond formation, while a value close to 0 represents bond fracture. (c) Variations of CN along the simulation time *t*; CN is clearly labeled in panel (d) of the IS and TS1 models. (d) The key structural models involved in AIMD simulation.

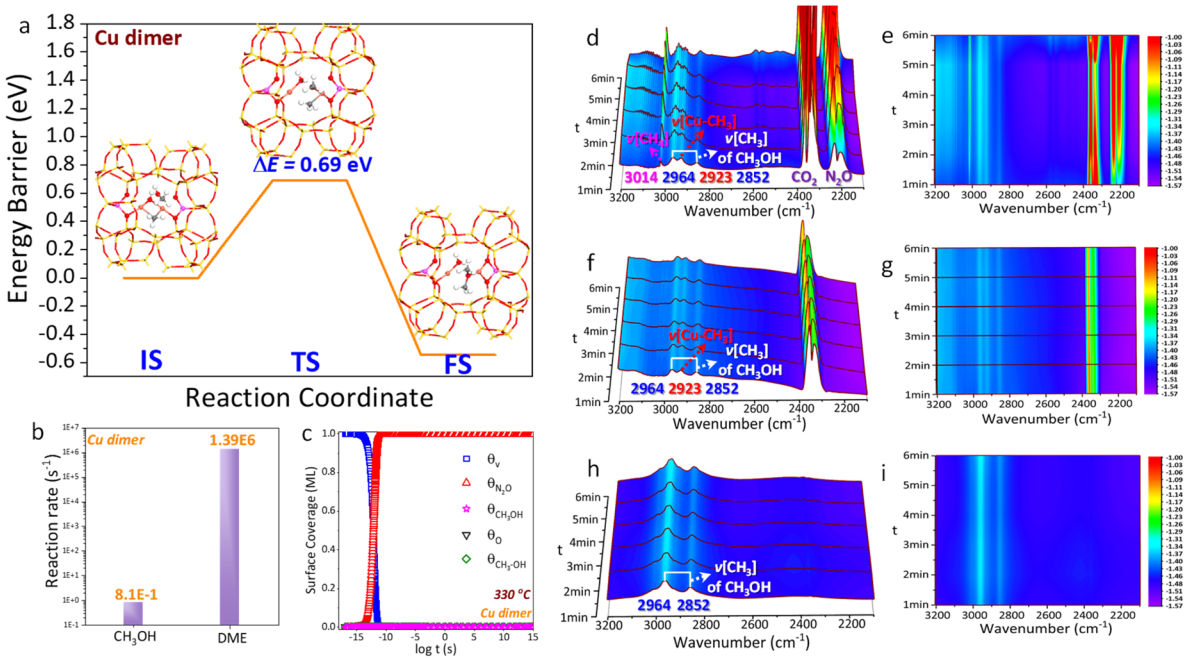

Fig. 6 DFT and *in situ* FTIR investigations on tandem catalysis of CH_3OH to form DME (CAS-DME route). (a) Derived energy diagram, (b) CH_3OH/DME net reaction rate comparison, and (c) surface coverage variations along the reaction time *t* over the Cu dimer site of Cu-FER; O red, Cu orange, Al pink, Si yellow, C gray, H white. (d and e) *In situ* FTIR results of cofeeding of CH_4 and N_2O (2% CH_4, 2% N_2O in He, 40 mL min^{-1}) over He pretreated Cu-FER-0.3%. (f and g) He sweeping (40 mL min^{-1}) after cofeeding and (h and i) introduction of CH_3OH (bubbled by He of 2 mL min^{-1}) after He sweeping at *T* of 250 °C; the Cu-FER-0.3% was initially pretreated with He for 1 h at 500 °C, then cooled down to 250 °C for the measurement.

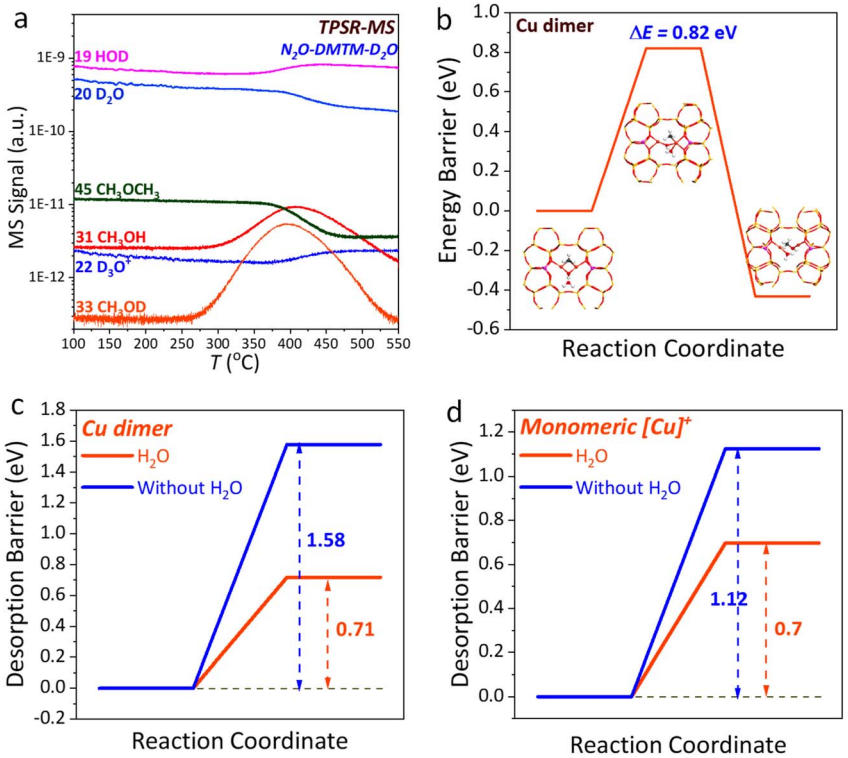

Fig. 7 Experimental and theoretical investigation on the effect of H_2O during N_2O-DMTM. (a) Isotopic transfer study during D_2O–N_2O-DMTM by TPSR-MS; (b) DFT simulated H_2O direct reaction route over the Cu dimer site (10 MR channel) of Cu-FER; energy diagram of H_2O-favored CH_3OH desorption over the (c) Cu dimer and (d) monomeric $[Cu]^+$ of Cu-FER.

mechanism. Upon co-feeding N_2O and CH_4, the radical of CH_3^- belonging to ν[Cu-CH_3] can be clearly observed at 2923 cm^{-1} (Fig. 6d and e) following the radical mechanism.[10] It could persist during subsequent He sweeping (Fig. 6f and g), which however nearly disappeared upon the further introduction of CH_3OH (Fig. 6h and i), leaving the strong ν[CH_3] bands of adsorbed CH_3OH (2964, 2852 cm^{-1}). This finding confirms the direct reaction of [Cu-CH_3] radical with CH_3OH. It should be noted that the minor production of DME and the overlap of ν[CH_3] with CH_3OH make it challenging to distinctly identify the generated DME. In this regard, we can deduce that the higher DME productivity relative to that of CH_3OH during N_2O-DMTM (Fig. 1d) can be majorly related to the tandem catalysis of CH_3OH principally over the Cu dimer site of 10 MR channel. Such reaction route would also significantly contribute to long-term reaction stability of Cu-FER-0.3% (Fig. S2a†), wherein the *in situ* generated CH_3OH functioning as a special "solvent" can react with the radicals of CH_3^- and OH^- to produce DME, which thereby would hinder carbon deposition caused by the accumulated radials of CH_3^-.

The H_2O could alter the reaction selectivity (Fig. 1d), resulting in CH_3OH as the major product, which can be closely related to two main reasons. The first one lies to that the H_2O could directly participate in DMTM reaction, consuming the generated radicals of CH_3^- and OH^- to form CH_3OH thereby significantly depressing DME production. As illustrated by TPSR-MS of Fig. 7a, the obvious signal increase of CH_3OD ($m/e = 33$) and HOD ($m/e = 19$) can be clearly observed along with the decreasing of D_2O ($m/e = 20$), which indicates the direct participation reaction of H_2O following the reaction route of (OH^- + D-OD + CH_3^- → HOD + CH_3OD). This can be well supported by the DFT simulation that the H_2O just needs crossing a low barrier (0.82 eV, Fig. 7b) to produce CH_3OH through directly reacting with the radicals of CH_3^- and OH^- over Cu dimer site. The second reason lies to that the H_2O could efficiently favor the desorption of CH_3OH with the desorption energy being extensively reduced from 1.58 to 0.71 eV (Fig. 7c) and 1.12 to 0.70 eV (Fig. 7d), respectively, over the Cu dimer and monomeric $[Cu]^+$ site. Thereby, the influence of H_2O during N_2O-DMTM over Cu-FER-0.3% can be well illustrated based on the combined D_2O isotopic tracer technique and DFT simulation. Meanwhile, the finding of H_2O significantly altering N_2O-DMTM selectivity can also well support the proposed CAS-DME route over Cu dimer site. As noted, it is also essential to discuss the influence of H_2O on the coordination environment of such dual Cu SA sites. As revealed by the *ab initio* thermodynamics (AIT) in our previous work,[10] H_2O complexation with the $[Cu]^+$ site actually cannot thermodynamically affect the methoxy formation to produce $[Cu–CH_3]^+$ and $[CuOH]^+$, due to its much lower thermodynamic stability. Moreover, H_2O complexations with $[Cu]^+$, $[CuOH]^+$ are reported to commonly occur under low temperature range (T < 300 °C) due to their weak thermodynamic stabilities.[55] In this regard, we can speculate that the influence of H_2O on the coordination environment of the dual Cu SA site in the present work would also be limited due to its low thermostability under our reaction conditions (T = 330 °C).

Reaction kinetics of diverse active sites

As for the intrinsic activity of monomeric $[Cu^+]$ and Cu dimer sites, the microkinetic modelling results (Fig. 3c) suggest a higher CH_3OH production rate of the monomeric $[Cu]^+$ site (8.7×10^1 s^{-1}) relative to the Cu dimer site (8.1×10^{-1} s^{-1}), which can be mainly related to the higher desorption barrier of CH_3OH over the Cu dimer site ($\Delta E = 1.58$ eV), although a relatively high N_2O dissociation barrier ($\Delta E = 1.35$ eV) can also be observed over the monomeric $[Cu^+]$ site. However, the production rate of DME over the Cu dimer site (1.39×10^6 s^{-1}, Fig. 6b) would be much higher than that of monomeric $[Cu]^+$ site (8.91×10^{-1}, Fig. S16b†) due to the extensively reduced barrier for the generated CH_3OH to produce DME ($\Delta E = 0.69$ eV, Fig. 6a) by following the CAS-DME route.

The production rate per Cu atom was further compared for the prepared Cu-FER samples (Fig. S21†). Cu-FER-0.11% exhibits the highest reaction rate per Cu atom of 144 233 mmol mol_{Cu}^{-1} h^{-1}. The Cu dimer proportion was further predicted based on EPR (Fig. 2e and S20†) and CO-probed *in situ* FTIR (Fig. 2c and S29†), which however indicates that the Cu-FER 0.11% possesses much lower Cu dimer content than Cu-FER-0.3% and Cu-FER-0.6% (see Table S14 and Fig. S29d†). Such discrepancy strongly implies the higher activity of Cu monomer, which also agrees well with our DFT and AIMD simulation results, showing that the dual Cu SA site, being categorized as Cu monomers as detailed in the ESI† (Identification Category of Dual Cu SA), functioned as the major active site rather than the Cu dimer. As revealed, CH_3OH would be primarily produced over the dual Cu SA site, which displays the highest kinetic reaction rate of 5.64×10^8 s^{-1} (Fig. 4f) relative to the 8.1×10^{-1} and 8.7×10^1 s^{-1} of Cu dimer and monomeric $[Cu]^+$ site, respectively. Herein, we would also like to note that being of a type of Cu monomer, it is still challenging to quantify the specific content of such dual Cu SA site. However, according to the TOF comparison results (Fig. S21†), we speculate that the Cu-FER with lower Cu loading of 0.11% would probably be much more favorable to form such dual Cu SA site, considering lower Cu loadings would favor Cu cation diffusion inside the FER channel.

As for DME, although it would be mainly generated over the Cu dimer site (located at 10 MR channel), displaying a high kinetic reaction rate of 1.39×10^6 s^{-1} (Fig. 6b), which is four orders of magnitude higher than that of the monomeric $[Cu]^+$ site (8.9×10^1 s^{-1}, Fig. S16b†), it is actually closely correlated with the *in situ* generated CH_3OH over the dual Cu SA site. In this regard, we can deduce that the dual Cu SA site would play a major role in deciding the reaction efficiency of Cu-FER, the specific content of which would be significantly determined by the distribution of framework Al. To make a further verification, Cu-FER-0.3%, with a higher SiO_2/Al_2O_3 ratio of 70, was further prepared by wet-ion-exchange method and evaluated for N_2O-DMTM (Fig. S27†). The derived reaction rate (represented by total productivity per gram of catalyst, 667.8 μmol g_{cat}^{-1} h^{-1}) is much lower than that of Cu-FER-0.3% ($SiO_2/Al_2O_3 = 30$), due to the increased SiO_2/Al_2O_3 ratio reducing the formation of such dual Cu SA active site. Therefore, based on the above results, we

can verify the significantly important kinetic role the dual Cu SA site plays during N_2O-DMTM over Cu-FER.

Finally, we would also like to mention that the H-FER zeolite, with the Fe impurity of 80–90 ppm, was also evaluated for N_2O-DMTM, displaying a relatively high and stable (CH_3OH + DME) productivity of 843 μmol g_{cat}^{-1} h^{-1} (average value of 6 h reaction). As investigated in our previous works, $Fe_{0.6\%}Cu_{0.68\%}$-BEA[56] and Fe-BEA-1.0%[6] display much lower CH_3OH productivity (~150 and 50 μmol g_{cat}^{-1} h^{-1}) and severe deactivation relative to H-FER during N_2O-DMTM in the absence of H_2O (under similar reaction conditions). Some other commercial H-zeolites (H-BEA, H-MOR, H-ZSM-5), which may also possess Fe impurities, have also been evaluated for N_2O-DMTM (see diagram below, further detailed in Fig. S28†), exhibiting much lower CH_3OH productivity (~10–80 μmol g_{cat}^{-1} h^{-1}) than H-FER. In this regard, we speculate that the Fe impurity would exert limited effect on N_2O-DMTM for the H-FER of the present work. Recently, Xiao *et al.*[8] investigated N_2O-DMTM over the transition-metal-free H-FER zeolite catalysts. After calcination at *T* of 850 °C, H-FER achieved a CH_3OH productivity as high as 18 300 μmol g_{cat}^{-1} h^{-1}. The distorted tetracoordinated framework Al and the pentacoordinated Al of the extra-framework were newly proposed to be the potential active centers generated during calcination, activation, and reaction. In this regard, we speculate that the relatively high productivity of 843 μmol g_{cat}^{-1} h^{-1} of H-FER can also be probably related to such AlO_x species. Due to the specific fundamental reaction mechanism was not present in ref. 8, such exploration based on DFT would be a good research point in future work.

Conclusion

The present work has developed an efficient continuous N_2O-DMTM system, achieving boosted productivity (58 368 mmol per mol_{Cu} per h of CH_3OH) over Cu-FER zeolite. A 2D spatial structure-favored tandem catalysis is presented for the first time. An unique dual Cu SA, located at the parallel 6 MR site (β site) of the 8 MR channel, was formed. It possesses much higher CH_3OH production efficiency (5.64×10^8 s^{-1}) than the traditional monomeric $[Cu]^+$ (8.7×10^1 s^{-1}) and Cu dimer sites (8.1×10^{-1} s^{-1}), which not only significantly reduces the N_2O dissociation barrier but also prevents the formation of less active oxo-Cu dimer sites $[Cu–O–Cu]^{2+}$. Additionally, favored the vertically interconnected 2D channel system of FER, the generated CH_3OH could readily diffuse into the 10 MR main channel for tandem catalysis to produce DME. Interestingly, functioning as a special "solvent," CH_3OH could directly react with the radicals of CH_3^- and OH^- to produce DME, which could efficiently hinder carbon deposition and guarantee the long-term stability of Cu-FER-0.3%. Notably, although Cu-FER possesses much higher N_2O-DMTM activity than Cu-BEA and Cu-MFI (Cu loading of 0.3%) with the 3D channel system, we still cannot conclude that the 2D channel system would be much more efficient than the 3D channel system for N_2O-DMTM. Based on the present study, we would like to emphasize that taking advantage of the zeolite spatial structure to control Cu active site distance would probably constitute a promising route for highly efficient N_2O-DMMT catalyst designs; additionally, preferring zeolite with a 2D channel system and suitable pore size can probably limit side reactions to enhance CH_3OH (or DME) selectivity.

Experimental and theoretical method

Catalyst preparation

The zeolite catalysts H-FER, H-BEA, H-MFI, and H-MOR, each with a Si/Al ratio of approximately 15, were procured from Nankai University Catalyst Co., Ltd, China. The Cu-zeolite samples, comprising Cu loadings of 0.11%, 0.3%, 0.6%, and 1.0% for Cu-FER, and 0.3% for Cu-BEA, Cu-MFI, and Cu-MOR, were synthesized *via* an ion-exchange method. Specifically, 5 g of H-zeolite and the requisite amount of $Cu(NO_3)_2 \cdot 6H_2O$ (Sigma-Aldrich) were combined in a round-bottom flask. This mixture was stirred at 400 rpm and maintained at a temperature of 100 °C for 6 h in the presence of 300 mL deionized water. Post-reaction, the slurry was filtered and rinsed multiple times with deionized water, then dried at 100 °C for 24 h. The final product was achieved through calcination at 550 °C for 4 h.

Characterizations

XRD, ICP, N_2 adsorption/desorption, XPS and TGA. The characterization of Cu-zeolite samples was conducted using a suite of analytical methods, including X-ray diffraction (XRD), inductively coupled plasma (ICP) emission spectrometry, nitrogen (N_2) adsorption/desorption, X-ray photoelectron spectroscopy (XPS), and thermogravimetric analysis (TGA). The crystal structures were determined *via* XRD, utilizing a Bruker D5005 diffractometer with a Cu Kα radiation source ($\lambda = 1.5406$ Å). ICP emission spectrometry, executed with a PerkinElmer Optima 7000DV, was used to assess the copper loadings. The samples' specific surface area and pore volume were analyzed through N_2 adsorption/desorption at −196 °C using a Sorptomatic 1990 instrument from Thermo Electron. Specific surface areas were calculated using the Brunauer–Emmett–Teller (BET) method, and micropore volume was determined by the *t*-plot method. XPS analysis was performed using a Thermo Fisher ESCALAB 250 system with Al Kα radiation under ultrahigh vacuum conditions. The binding energies were calibrated based on the C 1s energy of adventitious graphitic carbon at 284.8 eV.[38] The amount of deposited carbon (coke) was quantified with TGA using a NETZSCH TG209F1. A 10 mg sample was heated in an atmosphere containing 14% O_2 in N_2 (40 mL min^{-1}) at a heating rate of 5 °C min^{-1}, ranging from 50 to 1000 °C.

H_2-TPR, UV-vis, EPR and ^{27}Al NMR. The experimental methods employed in this study include H_2 temperature-programmed reduction (H_2-TPR), ultraviolet-visible diffuse reflectance spectroscopy (UV-vis DRS), electron paramagnetic resonance (EPR), and solid-state ^{27}Al nuclear magnetic resonance (NMR). The H_2-TPR analysis was performed using a fixed-bed reactor system integrated with a thermal conductivity detector (TCD) analyzer. A sample of 100 mg was reduced in an atmosphere containing 5% H_2 in Ar, across a temperature range of 100–800 °C, with a heating rate of 5 °C min^{-1}. Hydrogen

consumption was quantified using standard CuO (Sigma-Aldrich) as reference. For UV-vis DRS, measurements were conducted using a Shimadzu UV-2501PC spectrometer under ambient conditions. Diffuse reflectance spectra were calculated using the Kubelka–Munk function [$F(R) = (1 - R)^2/2R$]. The Cu-FER-0.3% was subjected to He and N_2O pretreatment strategies. For He pretreatment, Cu-FER-0.3% was exposed to a high-purity He stream (>99.999%, 40 mL min^{-1}) for 1 h at 500 °C, followed by cooling to room temperature in the same atmosphere. Under N_2O pretreatment, following initial He treatment, the sample was cooled to 250 °C and exposed to a 30% N_2O in He mixture (40 mL min^{-1}) for 1 h. EPR measurements were performed on a Bruker E580 X-band spectrometer to detect the presence and ratio of Cu dimers ($[Cu]^+$–$[Cu]^+$) on the Cu-FER samples. The same He and N_2O pretreatments as in the UV-vis DRS were applied. EPR experiments were conducted at −118 °C to reduce the mobility of Cu^{2+} ions, enabling resolution of their hyperfine structure. Notably, $[Cu]^+$–$[Cu]^+$ dimers can be readily oxidized into $[Cu–O–Cu]^{2+}$ upon N_2O pretreatment, resulting in no EPR signals. Therefore, the Cu dimer ratio can be estimated through quantitation of Cu^+ content over the Cu-FER samples being respectively pretreated by He and N_2O, following eqn (1), wherein η represents the estimated Cu dimer ratio; $n_{Cu^+–He}$ and $n_{Cu^+–N_2O}$ respectively represent the EPR-predicted spin concentration of Cu^+ over the He-pretreated and N_2O-pretreated samples of Cu-FER, as measured by the Spincount module within the Xenon software (Bruker, Germany). The specific values are listed in Table S14† and presented as counts per g. A similar quantification approach has also been reported in the literature.[39]

$$\eta = \frac{n_{cu^+eHe} - n_{cu^+eN_2O}}{n_{cu^+eHe}} \times 100\% \quad (1)$$

Solid-state ^{27}Al NMR spectra were acquired using a Bruker Avance 400 MHz spectrometer. The ^{27}Al chemical shift was referenced to −0.54 ppm with respect to $AlNH_4(SO_4)_2 \cdot 12H_2O$. Peak fitting was accomplished using MestReNova 14.0 software, with fitting parameters detailed in Table S11.†

X-ray absorption spectra (XAS). Cu K-edge XAS measurements were conducted at the BL14W1 beamline of the Shanghai Synchrotron Radiation Facility (SSRF) operated by the Shanghai Institute of Applied Physics (SINAP). The facility was operated at an energy level of 3.5 GeV with a maximum current of 250 mA. For measurements, a copper foil was utilized as a reference sample in transmission mode, while Cu-FER-0.3% was measured in fluorescence mode due to its low copper loading (~0.3 wt%). The XAS data were collected at room temperature and analyzed using the DEMETER software package (ATHENA and ARTEMIS)[40] for EXAFS analysis. The sample, weighing 100 mg, was prepared as a disc with a diameter of 10 mm and thickness of 1 mm. Prior to measurement, the sample underwent pretreatment with N_2O (30 vol% in He) at 250 °C for 3 h. The density functional theory (DFT) optimized structure depicted in Fig. S6,† featuring an oxo Cu dimer $[Cu–O–Cu]^{2+}$ active site motif structure was utilized for peak fitting in the extended X-ray absorption fine structure (EXAFS) analysis of Fig. 2i. Based on the XAS result, wavelet transform (WT) analysis was conducted *via* the HAMA software to provide a 2D representation of the EXAFS, revealing the signal features both in k and R-spaces, simultaneously. Thanks to the backscattering amplitude factor $F(k)$, which is closely correlated with atomic number, the WT analysis can overcome the indistinguishable overlap of R space. In particular, heavy atoms, having large values of $F(k)$, are located at higher k wavenumbers than lighter atoms.

***In situ* FTIR.** *In situ* Fourier transform infrared spectroscopy (*in situ* FTIR), using carbon monoxide (CO) as the probe molecule, was conducted using a Bruker Tensor II equipped with a mercury cadmium telluride (MCT) detector covering the range of 400–4000 cm^{-1}. Each spectrum was acquired with 32 scans at a resolution of 4 cm^{-1}. Approximately 20 mg of catalyst sample was compressed into a self-supporting wafer and placed into a microreactor with a calcium fluoride (CaF_2) infrared window. A pretreatment strategy involving helium (He) and nitrous oxide (N_2O), as previously described for UV-vis DRS and EPR characterization, was applied to Cu-FER-0.3 during the *in situ* FTIR experiment. Following pretreatment with He and N_2O, infrared signals were recorded every 30 s at 50 °C after introducing a CO mixture (1 vol% in He) into the system for 20 min. *In situ* FTIR was also applied in the mechanism investigations of N_2O-DMTM and DME, which are detailed in the ESI.†

D_2O isotopic tracer technique based on TPSR-MS. The D_2O isotopic tracer experiment was conducted based on temperature-programmed surface reaction (TPSR) over a fixed-bed reactor system and with the m/z signals of 16 (CH_4), 19 (HOD), 20 (D_2O), 22 $(D_3O)^+$, 31 (CH_3OH), 32 (O_2), 33 (CH_3OD), 44 (N_2O) and 45 (DME), as monitored by a mass spectrometer (NETZSCH QMS 403 D Aëolos). Initially, the catalyst sample of Cu-FER-0.3% (100 mg) was pretreated by He (>99.999%, 40 mL min^{-1}) for 1 h at 500 °C and then cooled to room temperature. During TPSR measurement (100–550 °C), the gas mixture of 2 vol% N_2O, 2 vol% CH_4 balanced by He (40 mL min^{-1}) was introduced into a glass flask to bubble the D_2O (T = 25 °C, Sigma-Aldrich, >99.96%) into the reactor, which was heated at a rate of 5 °C min^{-1}. The m/z signals were simultaneously recorded by the mass spectrometer through the multiple ion detection (MID).

Activity measurement

N_2O-DMTM activity measurement was carried out in a fixed-bed quartz reactor (outer diameter: 11 mm, inner diameter: 8 mm, length: 485 mm). The catalyst sample was pelletized into particles measuring 0.25–0.425 mm and packed into the constant-temperature zone of the reactor (0.5 g) using quartz wool plugs. Prior to measurement, the sample underwent pretreatment with He (>99.999%, 40 mL min^{-1}) for 1 h at 500 °C, followed by cooling to the reaction temperature of 330 °C. The reactant gases N_2O (>99.999%) and CH_4 (>99.999%), with He as the balance gas (>99.99%), were introduced into the system at a ratio of 30 : 15 : 55. An electronic mass flow meter adjusted the total flow rate to 100 mL min^{-1}, corresponding to a gas hourly space velocity (GHSV) of 12 000 h^{-1}. Heating *via* resistive tape maintained the entire gas line from the point of

liquid injection to the gas chromatography (GC) unit at 150 °C to prevent condensation. The GC loop (1 mL) was also heated at 150 °C within a valve box. The details are provided in the ESI.†

Computational method

Constructed model. Cu-FER models featuring monomeric $[Cu]^+$, Cu dimers, and dual Cu single-atom active sites (dual Cu SA site) were developed based on the H-FER framework obtained from the IZA. These models utilized lattice parameters of 19.16 × 14.13 × 7.49 Å.

DFT method. Periodic DFT calculations were carried out using the Vienna *Ab initio* Simulation Package (VASP).[41] The projector-augmented wave (PAW) method, combined with a plane-wave basis set with a cutoff energy of 400 eV, described the core and valence electrons.[42] The exchange–correlation functional was represented by the generalized gradient approximation (GGA) of Perdew and Wang (PW91).[43,44] Electronic energy convergence was set to 10^{-5} eV, and atomic forces were kept below 0.02 eV $Å^{-1}$ during both geometry optimization and transition state (TS) calculations. Transition states were determined using the climbing image nudged elastic band (CI-NEB) method[45] and validated by frequency calculations, showing only one imaginary frequency. The *k*-point sampling, done *via* the Monkhorst–Pack method,[46] was set to 2 × 2 × 1. Gibbs free energy computations were performed utilizing the VASPKIT software package.[47] Microkinetic modelling was conducted to illustrate the reaction efficiency of monomeric $[Cu]^+$ (Table S5†), Cu dimer (Table S6†) and dual Cu SA (Table S7†) sites to produce CH_3OH, as well as to calculate the DME production rate over the Cu dimer (Table S8†) and monomeric $[Cu]^+$ (Table S9†) sites. The specific elementary reaction steps, as well as the microkinetic parameters, are listed in Tables S5–S9.† The specific method can also be found in our previous work.[10]

CP2K-based AIMD for metadynamics simulations. *Ab initio* molecular dynamics (AIMD) simulations were conducted using the CP2K code,[48] incorporating spin-polarized DFT with the Perdew, Burke, and Ernzerhof (PBE) functional.[49] Wave functions were expanded using a molecularly optimized double-ζ Gaussian basis set to reduce basis set superposition errors, while an auxiliary plane-wave basis with a 400 Ry energy cutoff was employed for electrostatic energy computations. Scalar relativistic norm-conserving pseudopotentials were used to describe the core electrons,[50] and a semiempirical van der Waals correction (DFT-D3 scheme)[51] was applied to all calculations to account for long-range van der Waals dispersion interactions. AIMD-based metadynamic simulations were employed to illustrate N_2O-DMTM and BAS-DME route mechanisms by respectively taking the coordination numbers (CN) of CN_{Cu-O} and CN_{O-N} (see Fig. S19b†); CN_{C-H} and CN_{O-H} (see Fig. S19d†); and CN_{O-C} and $^aCN_{O-H}$ (see Fig. 5c) as the collective variables (CVs) in a canonical *NVT* ensemble ($T = 250$ °C) with a Nose–Hoover thermostat. The time step was set to 0.5 fs. CN was calculated according to eqn (2) ,[52] wherein d_{ij} is the internuclear distance of the atoms involved; d_0 is the threshold distance for bonding; p and q are exponents that determine the steepness of CN_{ij} decay with respect to d_{ij}.

$$CN_{ij} = \frac{1 - (d_{ij}/d_0)^p}{1 - (d_{ij}/d_0)^{p+q}} \quad (2)$$

The value of CN_{ij} varies from 0 to 1, respectively corresponding to bond breaking and bond formation. Eventually, the free energy surface diagrams in Fig. 4b–e, 5a and b were obtained based on the software PLUMED 2.[53]

CP2K-based AIMD for constrained MD simulations. We used CP2K-based AIMD for constrained molecular dynamics (MD) simulations to study the diffusion of methanol (CH_3OH) from an 8-member ring (8 MR) channel to a 10-member ring (10 MR) channel. Initially, bias-molecular mechanics (MM) MD simulations were performed with the O–Al distance (oxygen of CH_3OH and Al of the framework) as a collective variable at a temperature of 603 K to determine the complete diffusion pathway. Subsequently, constrained MD simulations, where the O–Al distance was fixed, were executed for selected configurations from the derived diffusion pathway within a canonical ensemble (*NVT*) at 603 K for 4 picoseconds (ps). The potential of mean force (PMF) was then calculated based on the average Lagrange multipliers from the Shake algorithm,[54] as detailed in Table S10.†

Data availability

The data supporting this study are available within the article and ESI.†

Author contributions

Ning Liu: writing – original draft, data curation, formal analysis, software. Tingting Zhang: investigation, methodology, software, visualization. Chengna Dai: data curation, resources, validation. Ruinian Xu:, methodology, conceptualization. Gangqiang Yu: data curation, validation, visualization. Ning Wang: resources, validation, visualization. Biaohua Chen: conceptualization, project administration, funding acquisition, supervision, writing – review and editing.

Conflicts of interest

There are no conflicts to declare.

Acknowledgements

We acknowledge the final support from the National Natural Science Foundation of China (No. 22176006).

Notes and references

1 N. F. Dummer, D. J. Willock, Q. He, M. J. Howard, R. J. Lewis, G. Qi, S. H. Taylor, J. Xu, D. Bethell, C. J. Kiely and G. J. Hutchings, *Chem. Rev.*, 2023, **123**, 6359–6411.
2 V. L. Sushkevich, D. Palagin, M. Ranocchiari and J. A. van Bokhoven, *Science*, 2017, **356**, 523–527.

3 P. Gupta, B. Rana, R. Maurya, R. Kalita, M. Chauhan and K. Manna, *Chem. Sci.*, 2025, **16**, 2785–2795.
4 W. Wang, W. Zhou, Y. Tang, W. Cao, S. R. Docherty, F. Wu, K. Cheng, Q. Zhang, C. Copéret and Y. Wang, *J. Am. Chem. Soc.*, 2023, **145**, 12928–12934.
5 T. Yu, Z. Li, W. Jones, Y. Liu, Q. He, W. Song, P. Du, B. Yang, H. An, D. M. Farmer, C. Qiu, A. Wang, B. M. Weckhuysen, A. M. Beale and W. Luo, *Chem. Sci.*, 2021, **12**, 3152–3160.
6 N. Liu, Y. Li, C. Dai, R. Xu, G. Yu, N. Wang and B. Chen, *J. Catal.*, 2022, **414**, 302–312.
7 J. Xie, R. Jin, A. Li, Y. Bi, Q. Ruan, Y. Deng, Y. Zhang, S. Yao, G. Sankar, D. Ma and J. Tang, *Nat. Catal.*, 2018, **1**, 889–896.
8 P. Xiao, Y. Wang, Y. Lu, K. Nakamura, N. Ozawa, M. Kubo, H. Gies and T. Yokoi, *J. Am. Chem. Soc.*, 2024, **146**, 10014–10022.
9 G. Zhao, P. Yan, K. Procter, A. Adesina, Y. Jin, E. Kennedy and M. Stockenhuber, *J. Catal.*, 2023, **417**, 140–152.
10 R. Xu, N. Liu, C. Dai, Y. Li, J. Zhang, B. Wu, G. Yu and B. Chen, *Angew. Chem., Int. Ed.*, 2021, **60**, 16634–16640.
11 G. Zhao, K. Chodyko, E. Benhelal, A. Adesina, E. Kennedy and M. Stockenhuber, *J. Catal.*, 2021, **400**, 10–19.
12 I. Gokce, M. O. Ozbek and B. Ipek, *J. Catal.*, 2023, **427**, 115113.
13 B. Yu, L. Cheng, S. Dai, Y. Jiang, B. Yang, H. Li, Y. Zhao, J. Xu, Y. Zhang, C. Pan, X.-M. Cao, Y. Zhu and Y. Lou, *Adv. Sci.*, 2023, **10**, 2302143.
14 Á. Szécsényi, G. Li, J. Gascon and E. A. Pidko, *Chem. Sci.*, 2018, **9**, 6765–6773.
15 Y. Deng, H. Lei, U. Simon, D. Ye and P. Chen, *ACS Catal.*, 2024, **14**, 292–298.
16 L. N. Wilcox, J. Rebolledo-Oyarce, A. D. Mikes, Y. Wang, W. F. Schneider and R. Gounder, *ACS Catal.*, 2024, **14**, 3647–3663.
17 X. Tang, J. Ye, L. Guo, T. Pu, L. Cheng, X.-M. Cao, Y. Guo, L. Wang, Y. Guo, W. Zhan and S. Dai, *Adv. Mater.*, 2023, **35**, 2208504.
18 H. Zhang, P. Han, D. Wu, C. Du, J. Zhao, K. H. L. Zhang, J. Lin, S. Wan, J. Huang, S. Wang, H. Xiong and Y. Wang, *Nat. Commun.*, 2023, **14**, 7705.
19 S. Grundner, M. A. C. Markovits, G. Li, M. Tromp, E. A. Pidko, E. J. M. Hensen, A. Jentys, M. Sanchez-Sanchez and J. A. Lercher, *Nat. Commun.*, 2015, **6**, 7546.
20 I. Lee, M.-S. Lee, L. Tao, T. Ikuno, R. Khare, A. Jentys, T. Huthwelker, C. N. Borca, A. Kalinko, O. Y. Gutiérrez, N. Govind, J. L. Fulton, J. Z. Hu, V.-A. Glezakou, R. Rousseau, M. Sanchez-Sanchez and J. A. Lercher, *JACS Au*, 2021, **1**, 1412–1421.
21 A. J. Knorpp, A. B. Pinar, C. Baerlocher, L. B. McCusker, N. Casati, M. A. Newton, S. Checchia, J. Meyet, D. Palagin and J. A. van Bokhoven, *Angew. Chem., Int. Ed.*, 2021, **60**, 5854–5858.
22 K. Mlekodaj, M. Lemishka, A. Kornas, D. K. Wierzbicki, J. E. Olszowka, H. Jirglová, J. Dedecek and E. Tabor, *ACS Catal.*, 2023, **13**, 3345–3355.
23 E. Tabor, J. Dedecek, K. Mlekodaj, Z. Sobalik, P. C. Andrikopoulos and S. Sklenak, *Sci. Adv.*, 2020, **6**, eaaz9776.
24 P. Xiao, Y. Wang, L. Wang, H. Toyoda, K. Nakamura, S. Bekhti, Y. Lu, J. Huang, H. Gies and T. Yokoi, *Nat. Commun.*, 2024, **15**, 2718.
25 J. Wang, J. Zhang, C. Xing, T. Jin, J. Liu, M. Ju and X. Tang, *Chem. Eng. J.*, 2023, **455**, 140379.
26 J. Ohyama, Y. Tsuchimura, A. Hirayama, H. Iwai, H. Yoshida, M. Machida, S. Nishimura, K. Kato and K. Takahashi, *ACS Catal.*, 2022, **12**, 2454–2462.
27 M.-L. Tsai, R. G. Hadt, P. Vanelderen, B. F. Sels, R. A. Schoonheydt and E. I. Solomon, *J. Am. Chem. Soc.*, 2014, **136**, 3522–3529.
28 P. Vanelderen, B. E. R. Snyder, M.-L. Tsai, R. G. Hadt, J. Vancauwenbergh, O. Coussens, R. A. Schoonheydt, B. F. Sels and E. I. Solomon, *J. Am. Chem. Soc.*, 2015, **137**, 6383–6392.
29 C. Negri, T. Selleri, E. Borfecchia, A. Martini, K. A. Lomachenko, T. V. W. Janssens, M. Cutini, S. Bordiga and G. Berlier, *J. Am. Chem. Soc.*, 2020, **142**, 15884–15896.
30 J. Tuo, J. Wang, X. Gong, C. Zhai, H. Xu, T. Xue, J. Jiang, Y. Guan and P. Wu, *Fuel*, 2024, **357**, 130001.
31 Z. Xiong, G. Qi, L. Bai, E. Zhan, Y. Chu, J. Xu, N. Ta, A. Hao, F. Deng and W. Shen, *Catal. Sci. Technol.*, 2022, **12**, 4993–4997.
32 C. Dai, Y. Zhang, N. Liu, G. Yu, N. Wang, R. Xu and B. Chen, *Phys. Chem. Phys. Chem.*, 2023, **25**, 24894–24903.
33 K. Jíša, J. Nováková, M. Schwarze, A. Vondrová, S. Sklenák and Z. Sobalik, *J. Catal.*, 2009, **262**, 27–34.
34 S. Sklenak, P. C. Andrikopoulos, B. Boekfa, B. Jansang, J. Nováková, L. Benco, T. Bucko, J. Hafner, J. Dědeček and Z. Sobalík, *J. Catal.*, 2010, **272**, 262–274.
35 J. E. Olszówka, P. Kubat, J. Dedecek and E. Tabor, *J. Phys. Chem. C*, 2023, **127**, 7344–7351.
36 A. J. Jones and E. Iglesia, *Angew. Chem., Int. Ed.*, 2014, **53**, 12177–12181.
37 G. Marsden, P. Kostetskyy, R.-S. Sekiya, A. Hoffman, S. Lee, R. Gounder, D. Hibbitts and L. J. Broadbelt, *ACS Mater. Au*, 2022, **2**, 163–175.
38 R. Xu, Z. Wang, N. Liu, C. Dai, J. Zhang and B. Chen, *ACS Catal.*, 2020, **10**, 6197–6212.
39 I. D. N. Jugniot, A. Rivot, P. Massot, C. Cardiet, A. Pizzoccaro, M. Jean, N. Vanthuyne, J.-M. Franconi, P. Voisin, G. Devouassoux, E. Parzy, E. Thiaudiere, S. R. A. Marque, A. Bentaher, G. Audran and P. Mellet, *Free Radical Biol. Med.*, 2018, **126**, 101–112.
40 B. Ravel and M. Newville, *J. Synchrotron Radiat.*, 2005, **12**, 537–541.
41 G. Kresse and J. Furthmüller, *Phys. Rev. B: Condens. Matter Mater. Phys.*, 1996, **54**, 11169–11186.
42 G. Kresse and D. Joubert, *Phys. Rev. B: Condens. Matter Mater. Phys.*, 1999, **59**, 1758–1775.
43 Y. Wang and J. P. Perdew, *Phys. Rev. B: Condens. Matter Mater. Phys.*, 1991, **44**, 13298–13307.
44 J. P. Perdew, J. A. Chevary, S. H. Vosko, K. A. Jackson, M. R. Pederson, D. J. Singh and C. Fiolhais, *Phys. Rev. B: Condens. Matter Mater. Phys.*, 1992, **46**, 6671–6687.
45 G. Henkelman, B. P. Uberuaga and H. Jónsson, *J. Chem. Phys.*, 2000, **113**, 9901–9904.

46 H. J. Monkhorst and J. D. Pack, *Phys. Rev. B*, 1976, **13**, 5188–5192.
47 V. Wang, N. Xu, J. Liu, G. Tang and W. Geng, *arXiv*, 2019, preprint, arXiv:1908.08269, DOI: 10.48550/arXiv.1908.08269.
48 J. Hutter, M. Iannuzzi, F. Schiffmann and J. VandeVondele, *Wiley Interdiscip. Rev.: Comput. Mol. Sci.*, 2014, **4**, 15–25.
49 J. P. Perdew, K. Burke and M. Ernzerhof, *Phys. Rev. Lett.*, 1996, **77**, 3865–3868.
50 S. Goedecker, M. Teter and J. Hutter, *Phys. Rev. B: Condens. Matter Mater. Phys.*, 1996, **54**, 1703–1710.
51 S. Grimme, J. Antony, S. Ehrlich and H. Krieg, *J. Chem. Phys.*, 2010, **132**, 154104.
52 L. Petersen, A. Ardèvol, C. Rovira and P. J. Reilly, *J. Am. Chem. Soc.*, 2010, **132**, 8291–8300.
53 G. A. Tribello, M. Bonomi, D. Branduardi, C. Camilloni and G. Bussi, *Comput. Phys. Commun.*, 2014, **185**, 604–613.
54 G. Ciccotti, M. Ferrario, J. T. Hynes and R. Kapral, *Chem. Phys.*, 1989, **129**, 241–251.
55 C. Paolucci, A. A. Parekh, I. Khurana, J. R. Di Iorio, H. Li, J. D. Albarracin Caballero, A. J. Shih, T. Anggara, W. N. Delgass, J. T. Miller, F. H. Ribeiro, R. Gounder and W. F. Schneider, *J. Am. Chem. Soc.*, 2016, **138**, 6028–6048.
56 Y. Li, N. Liu, C. Dai, R. Xu, G. Yu, N. Wang, J. Zhang and B. Chen, *Catalysts*, 2021, **11**, 1444.